Theoretical analysis of thermally tunable microring resonator filters made of dielectric-loaded plasmonic waveguides

Odysseas Tsilipakos,[a] Traianos V. Yioultsis, and Emmanouil E. Kriezis[a]
Department of Electrical and Computer Engineering, Aristotle University of Thessaloniki, Thessaloniki GR-54124, Greece

(Received 24 July 2009; accepted 30 September 2009; published online 10 November 2009)

Microring resonator filters, which are made of dielectric-loaded surface plasmon polariton waveguides and operate in the telecom spectral range, are thoroughly analyzed by means of vectorial three dimensional (3D) finite element method (FEM) simulations. The filters' functional characteristics, such as the resonant frequencies where the transmission minima occur, the free spectral range, the extinction ratio, and the minima linewidth associated with the quality factor of the resonances, are investigated for different values of the key structural parameters, namely, the ring radius and the gap separating the bus waveguide from the ring. The rigorous 3D-FEM simulations are qualitatively complemented by a simplified model. Apart from the harmonic propagation simulations, the uncoupled microring is treated as an eigenvalue problem, and the frequencies of the resonances are compared with those of the transmission minima. Furthermore, the possibility of exploiting the thermally tuned microring resonator filter as a switching element is explored. The shift in the transmission minima is quantified when the ring's refractive index is altered by virtue of Ohmic heating, and in addition to that, the temporal response is assessed by solving the transient problem. © *2009 American Institute of Physics*. [doi:10.1063/1.3256139]

I. INTRODUCTION

During the last few years, significant research effort has been directed to the field of plasmonics, i.e., a branch of nanophotonics concerned with the manipulation and routing of surface plasmon polaritons (SPPs). SPPs are electromagnetic surface waves coherently coupled to free electron oscillations.[1] They propagate along a metal-dielectric interface and exhibit an exponential decay of the field components away from it. Plasmonic waveguides comprising one or more metal-dielectric interfaces can confine light in subwavelength lateral dimensions, thus breaking the barrier set in conventional optical waveguides by the diffraction limit. As a result, plasmonic components are a prime candidate for nanophotonic integrated circuits since they can combine the immense bandwidth/operating speed of photonics along with reduced physical scale, resembling that of very large scale integrated electronics.[2–6]

In the past years, several types of plasmonic waveguides have been demonstrated in a pursuit of a favorable compromise between lateral confinement and propagation losses; a fundamental trade-off in plasmonics. The stripe[7,8] and channel[9,10] plasmonic waveguides were the first to be extensively investigated, and each of them has been employed in the implementation of a broad range of passive components that are able to manipulate light waves in desirable ways, i.e., to change the direction, split the power, or filter the light wave. Among the recently proposed waveguiding structures, the dielectric-loaded surface plasmon polariton (DLSPP) waveguide[11–13] offers some distinct advantages. It is technologically simple, consisting of a dielectric ridge deposited on a metallic film; it exhibits strong guiding properties, allowing for bend elements a few micrometers long with negligible bend losses,[14] thus serving the purposes of densely integrated plasmonic circuits; and finally, the propagation losses due to resistive damping in the metallic film are relatively low. Another significant advantage of the DLSPP waveguide is that the dielectric ridge can be readily replaced by a thermo-optic, electro-optic, or nonlinear material, thus enabling the realization of dynamic components that can be externally tuned by means of an electrical or optical control signal.

As was the case with other plasmonic waveguides, the DLSPP waveguide has been employed in the implementation of several passive components, which have been experimentally characterized and numerically investigated.[14,15] These include waveguide bends, coupled lines, and splitters. More recently, interest has been focused on wavelength-selective components, i.e., a special class of passive components whose response depends strongly on the wavelength of the input signal. Wavelength-selective components are important in plasmonics since they can extend the functionality offered by plasmonic circuits. What is more, they provide the basis for the realization of dynamically controlled components. Very recently, wavelength-selective components based on the DLSPP waveguide, namely, Bragg reflectors, Mach–Zehnder interferometers, directional couplers, and microring resonator filters, have been demonstrated.[15–18]

In this work we focus on the microring resonator filter, which seems to be the most promising of the DLSPP-based wavelength-selective components. Although the main attributes of microring resonator filter performance have been outlined,[17,18] a thorough numerical analysis has yet to be conducted. To this end, we perform rigorous three dimensional finite element method (3D-FEM) simulations in order to obtain a deeper insight on how the key structural param-

[a]Electronic addresses: otsilipa@auth.gr and mkriezis@auth.gr.

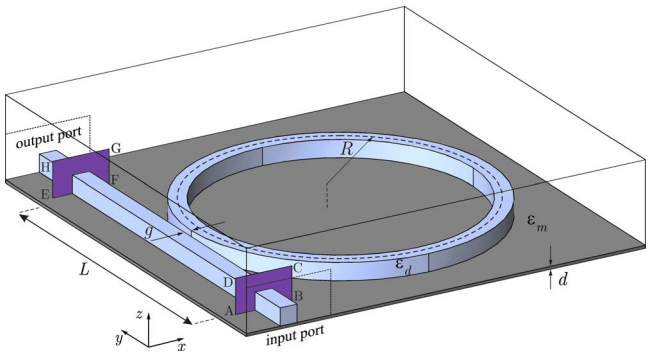

FIG. 1. (Color online) Schematic of a DLSPP-based microring resonator filter. The cross section at which the output power is calculated is marked as EFGH and is separated by a distance L from plane ABCD at which the reference power is calculated in the absence of the ring.

eters, namely, the ring radius and the gap separating the waveguide from the ring, affect the filter performance. In addition, the tuning of thermally addressed DLSPP-based microring resonator filters is considered. This paper is organized as follows: In Sec. II the operating principle and structural layout of the microring resonator filters considered in the simulations are presented. Section III introduces the details of the finite element method and discusses the results obtained from both harmonic propagation and eigenvalue simulations. The possibility of exploiting the thermally tuned filter as a switching element is explored in Sec. IV. Thermal modeling simulations are conducted for both the steady-state and transient problems. Finally, in Sec. V, we summarize the key performance characteristics of the DLSPP-based microring resonator filters and provide some concluding remarks.

II. MICRORING RESONATOR FILTERS: OPERATING PRINCIPLE AND STRUCTURAL LAYOUT

The microring resonator filter is composed of a bus waveguide coupled to a microring resonator (Fig. 1). A portion of the power propagating in the waveguide is coupled to the ring, depending on the gap separating the two and the interaction length determined by the shape and radius of the ring. The filter transmission, i.e., the power propagating in the straight waveguide past the resonator, is dictated by the result of interference between the circulating mode and the mode that continues to propagate in the straight waveguide instead of coupling to the ring. Its pattern with respect to the free-space wavelength is expected to be comblike, with the transmission minima corresponding to resonances of the microring. Assuming that the coupling between the waveguide and the ring is lossless, that a single unidirectional mode is excited in the ring, and that no reflections are present, one can end up with a simplified model for the microring resonator filter.[19] We note that the simplified model does not take into account, among others, the distributed nature of the coupling region nor the scattering losses therein. In order to describe the lumped coupling region, we adopt a scattering matrix of the form[22]

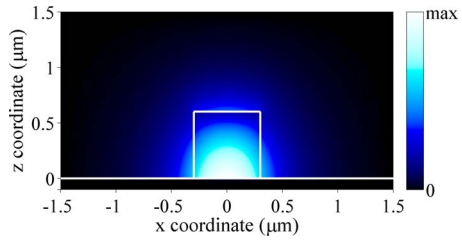

FIG. 2. (Color online) TM_{00} guided mode of the DLSPP waveguide, which consists of a 600×600 nm^2 polymer ridge deposited on a 70-nm-thick gold film. The E_z component is depicted for an operating wavelength of 1.55 μm. The field enhancement near the metal-dielectric interface is evident.

$$e^{j\theta_0}\begin{bmatrix} t & j\sqrt{1-|t|^2} \\ j\sqrt{1-|t|^2} & t^* \end{bmatrix}. \tag{1}$$

The phase factor $\exp(j\theta_0)$ renders the matrix valid for more than one frequency. In Ref. 19 this factor is omitted by virtue of a particular choice of the reference planes valid for a single frequency. We also note that the matrix is symmetrical (equal off-diagonal elements) only for a coupler that possesses a certain mirror plane. In our case this mirror plane is the xz plane bisecting the ring (with respect to the coordinate system of Fig. 1). On the other hand, the absence of a second mirror plane (a yz one) prevents the diagonal elements from being equal. The transmission is given by the following expression:

$$T=\frac{\alpha^2+|t|^2-2\alpha|t|\cos[\theta-(\theta_0-\theta_t)]}{1+\alpha^2|t|^2-2\alpha|t|\cos[\theta-(\theta_0-\theta_t)]}. \tag{2}$$

In the above equation, θ is the phase accumulated by the mode in the ring per circulation and α stands for the loss in the ring, comprising both propagation and bend losses. Consequently, after one roundtrip, the field amplitude of the circulating mode is scaled by the complex factor $\alpha\exp(-j\theta)$, where $\theta=(2\pi/\lambda)\mathrm{Re}[n_{\mathrm{eff}}(\lambda)](2\pi R)$ and R is the ring radius. Finally, t is a complex coefficient, $t=|t|\exp(j\theta_t)$. To prevent any confusion that may be caused by the direct comparison of Eq. (2) with Eq. (5) of Ref. 19, we note that in the latter a minus sign should appear in front of θ. Equation (2) will be used to qualitatively complement the rigorous 3D-FEM simulations throughout Secs. III A and III B.

Regarding the microring resonator filters considered in the simulations, both the bus waveguide and the ring are made of a $w\times h=600\times600$ nm^2 polymer ridge deposited on a $d=70$-nm-thick gold film (Fig. 1). The dimensions of the ridge ensure the single-mode operation of the DLSPP waveguide in the wavelength range of interest.[13] For simulation purposes, no substrate on which the gold film is deposited needs to be considered due to the limited penetration of light in the gold film. Specifically, for wavelengths in the neighborhood of 1.55 μm, the thickness of 70 nm is more than adequate for the exponentially decaying tail of the TM_{00} mode (the fundamental mode supported by the DLSPP waveguide) to entirely fade before reaching the bottom face of the metallic film (Fig. 2). The remaining geometrical parameters are the gap separating the waveguide from the ring (measured between the edges of the two) g and the ring radius R.

They will be regarded as design parameters, acquiring different values in the following simulations. Finally, concerning the material properties, the polymer has a typical refractive index of 1.5362 ($\varepsilon_r = 2.36$), and the dielectric permittivity of gold is obtained by linear interpolation between the measured values reported in Ref. 20.

III. NUMERICAL MODELING

The 3D vector finite element method[21] has been utilized for the numerical analysis of the microring resonator filters. All simulations were conducted by using in-house code. Triangular prism (edge) elements of the first order in both transverse and longitudinal directions were used for the discretization of the vector Helmholtz equation

$$\nabla \times \bar{\bar{\mu}}_r^{-1} \times \mathbf{E} - k_0^2 \bar{\bar{\varepsilon}}_r \mathbf{E} = 0. \tag{3}$$

The choice of the aforementioned elements is justified by the planar nature of the structure and leads to a reduced number of degrees of freedom (DoFs). Absorbing boundary conditions (ABCs) of the first order were implemented for the truncation of the computational domain on all sides and the top of the bounding box and in addition to that, a perfectly matched layer (PML) with a quadratic profile was employed for the reflectionless termination of the bus waveguide. The PML is only locally employed, where the absorption requirements are pronounced; its universal utilization would lead to a significant increase in the DoFs and would degrade the conditioning of the finite element matrices. We also note that the ABCs corresponding to the input and output ports of the straight waveguide are slightly modified in order to account for the coordinate-dependent wave impedance, $Z_w(x,z)$, of the TM_{00} mode. This is not trivial because the ordinary ABCs are designed for TEM, TM, or TE modes[21] (constant wave impedance), while the fundamental mode supported by the DLSPP waveguide is a hybrid one (TM-like). By applying the finite element method we can solve for the E-field in the entire structure. Figure 3 lucidly demonstrates filter operation at a transmission minimum ($\lambda = 1.594$ μm) and the neighboring maximum ($\lambda = 1.568$ μm).

A. Effect of gap

The effect of the gap that separates the bus waveguide from the ring g on the filter transmission is investigated by appointing different values to the gap, i.e., 0.3, 0.25, and 0.2 μm, respectively, and recording the transmission in the telecom range: 1.49–1.61 μm. The ring radius is fixed at 5 μm. Specifically, after exciting the TM_{00} mode in the input port of the straight waveguide, guided power still propagating in the bus waveguide past the ring resonator is collected at the fictitious plane EFGH (Fig. 1) and normalized with respect to a reference power level. This reference level is calculated by simulating a single waveguide, i.e., omitting the ring, and collecting the propagating power at the fictitious plane ABCD (Fig. 1). In the presence of the ring, the mode propagating in the straight waveguide toward the ring is disturbed by bend losses as well as any counterpropagating modes, and hence the additional simulations of the single waveguide are necessary for a reference power level to be

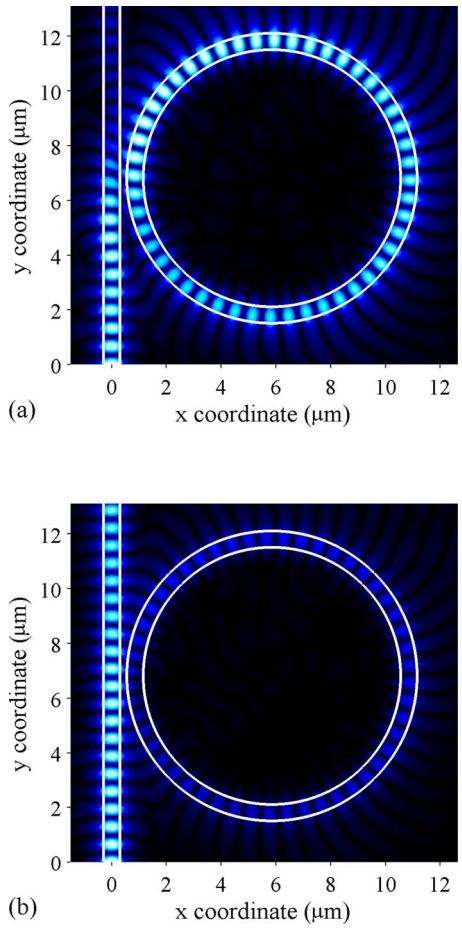

FIG. 3. (Color online) Absolute value of real part of E_z ($|\mathrm{Re}[E_z]|$) (a) at a transmission minimum ($\lambda = 1.594$ μm) and (b) at a transmission maximum ($\lambda = 1.568$ μm). The E_z component is plotted at an xy plane located 10 nm above the metal surface. The ring radius is 5 μm and the gap is equal to 0.25 μm.

specified. Planes ABCD and EFGH are $L = 11$ μm apart (Fig. 1). This length L alone introduces a power loss of $\exp(-L/L_{\mathrm{prop}})$, where L_{prop} is the propagation length for the TM_{00} mode and is approximately equal to 42 μm in the vicinity of 1.55 μm, thus limiting the maximum transmission to a value of 0.77. It follows that for a direct comparison with the simplified model to be possible, a scaling term of $\exp(-L/L_{\mathrm{prop}})$ must be incorporated in Eq. (2).

As can be seen from the results of the simulations (Fig. 4), the gap mainly influences the extinction ratio of the filter, i.e., contrast between minimum and maximum of transmission, while leaving the positions of the transmission minima, the free spectral range (FSR), and the passband bandwidth almost unaffected. The respective extinction ratios for the three cases are 7.35, 10.5, and 17 dB. The maxima are typically flat, while the minima are sharp with the linewidth being approximately 10 nm when measured at the −3 dB points ($g = 0.2$ μm). Furthermore, we observe that for a fixed gap the contrast increases with wavelength, as was also reported in Ref. 17.

It is important to check whether the trend of improving extinction ratios with decreasing gap revealed from the simulations is consistent with the simplified model described by Eq. (2). To perform a comparison between the two, let us

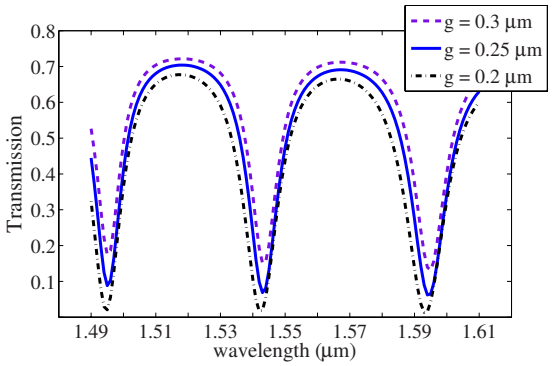

FIG. 4. (Color online) Transmission vs wavelength for different values of the gap separating the bus waveguide from the ring. The ring radius is equal to 5 μm. The respective extinction ratios in the three cases are 7.35, 10.5, and 17 dB.

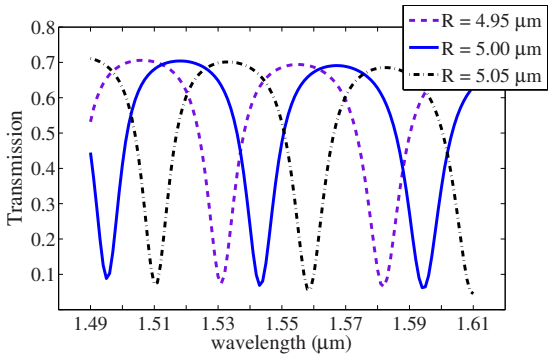

FIG. 5. (Color online) Transmission vs wavelength for slight variations in the ring radius. A variation of 50 nm results in a shift of up to 15 nm. The gap is fixed at 0.25 μm.

begin by providing a realistic estimate for the parameters α and $|t|$ of the simplified model (the case of $g=0.25$ μm is examined). If we were to momentarily disregard the bend losses, then the resistive losses alone would set an upper bound on α. Clearly, the value of this upper bound is $\exp(-2\pi R/2L_{\text{prop}}) \approx 0.69$. The factor of 2 is included in the denominator of the exponent because α refers to the field amplitude, while L_{prop} is the propagation length at which the optical power has dropped to $1/e$. With the contribution of the bend losses, expected to be relatively low in the 5 μm radius case, α will be somewhat lowered with respect to the upper limit of 0.69. On the other hand, $|t|$ is expected to be rather high. To back this up, we simulated two straight coupled DLSPP waveguides separated by a gap of 0.25 μm. The coupling length at which all of the power is coupled to the second waveguide is found to be 7.2 μm. The interaction length in the case of the microring resonator filter is substantially smaller, and the gap between the waveguide and the ring constantly increases from the minimum value of 0.25 encountered at the center of the interaction region. We therefore expect that most of the power propagating in the straight waveguide will continue to do so instead of coupling to the ring. Indeed, a value of 0.85 for $|t|$—along with a value of 0.69 for α—reproduces the transmission curve obtained by the finite element simulation quite well.

We now proceed to the verification of the aforementioned trend. By decreasing the gap, more power is coupled to the ring and the parameter t decreases in magnitude. One can easily confirm that when in the $|t|>\alpha$ regime, substituting decreasing values of $|t|$ in Eq. (2) while keeping α constant leads to improved extinction ratios. In other words, by decreasing $|t|$ we approach critical coupling ($|t|=\alpha$) where the transmission vanishes and the extinction ratio is greatly improved.

B. Effect of ring radius

Another key structural parameter of the microring resonator filter is the radius of the ring. By keeping the gap fixed at 0.25 μm and by slightly varying the radius, the minima of the transmission are shifted (Fig. 5) due to the different amounts of phase θ accumulated per circulation. In fact, the positions of the minima are quite sensitive to the variation in the radius, with a variation of 50 nm resulting in a shift of up to 15 nm. Varying the ring radius is a means of changing the ring's optical path length. Alternatively, one could modify the refractive index of the ring. Again, this would result in a shift in the transmission minima or, equivalently, the tuning of the filter. Thermal tuning of microring resonator filters will be addressed in Sec. IV.

However, a variation in this order of magnitude has a negligible effect on the other transmission properties of the filter, namely, the FSR, passband bandwidth, and extinction ratio. With respect to the simplified model, this can be explained by the fact that the parameters α and t just barely change. In order to demonstrate a filter with a substantially modified FSR we have modeled a ring with a radius of 3.5 μm (Fig. 6). Indeed, in this case the FSR is approximately 70 nm as opposed to 50 nm of the 5 μm ring. The passband bandwidth is also considerably affected, as well as the linewidth of the minima, associated with the quality factor of the ring resonances, and the extinction ratio.

We can explain the degradation of the extinction ratio by means of the simplified model as follows. In Sec. III A we argued that in the 5 μm radius case the filter was operating in the $|t|>\alpha$ regime. As can be seen from Fig. 6, the 3.5 μm ring resonator filter is further away from critical coupling than its 5 μm counterpart. This can be attributed to an in-

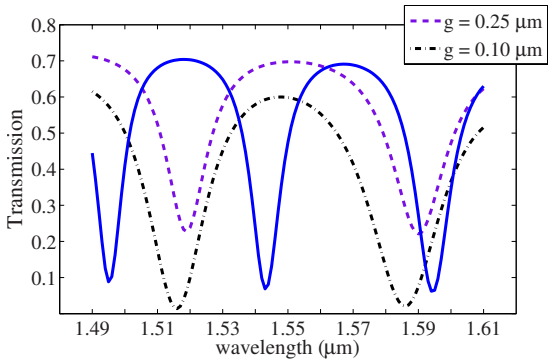

FIG. 6. (Color online) Transmission vs wavelength for a microring resonator filter having a radius of 3.5 μm. The FSR is ~70 nm as opposed to ~50 nm of the 5 μm ring. Two values for the gap are considered: $g=0.25$ μm and $g=0.1$ μm. In the latter case, the extinction ratio is improved and reaches the value of 17 dB. The reference case of $R=5$ and $g=0.25$ μm is included (solid line) to facilitate comparison.

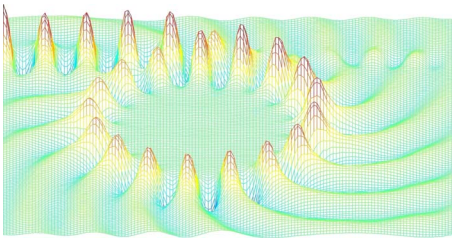

FIG. 7. (Color online) Augmented bend losses in the case of $R=3.5$ μm ($g=0.1$ μm). The real part of E_z is depicted at an xy plane 10 nm above the metal surface. The operating wavelength is 1.586 μm corresponding to a transmission minimum.

crease in $|t|$ due to the reduced interaction length and a decrease in α due to the augmented bend losses (in Sec. III C we confirm through eigenvalue simulations that the 3.5 μm ring is indeed lossier). Specifically, the bend losses per circulation in this case of smaller radius are considerably increased (Fig. 7) and cannot be balanced out by the reduced resistive losses.

We can compensate for the degradation of the extinction ratio by decreasing the gap. In this case, more power is coupled to the ring and the parameter t decreases in magnitude too. Since we are still in the $|t|>\alpha$ regime, by lowering $|t|$ we approach critical coupling, where the transmission vanishes. The filter transmission for the case of $g=0.1$ μm is included in Fig. 6. The extinction ratio is improved and reaches the value of 17 dB, matching the performance of the 5 μm ring filter. Therefore, the 3.5 μm ring filter, being much more compact than its 5 μm ring counterpart, appears to be an attractive option for densely integrated circuits, provided that one can tolerate the slightly higher insertion loss, the broader linewidth of the transmission minima, and the technological challenge of the 100 nm gap.

C. The uncoupled microring resonator: An eigenvalue problem

In this section, in an attempt to corroborate the findings of the harmonic propagation simulations, we treat the uncoupled microring resonator as a 3D eigenvalue problem. By utilizing the finite element method, we formulate a quadratic eigenvalue problem for a standalone microring resonator surrounded by ABCs. Subsequently, we linearize the quadratic problem and solve the corresponding (generalized) linear one. To obtain an admissible solution, we consecutively redefine the linearization point until the eigenvalue converges. From the complex eigenvalues we can identify the resonant wavelengths and calculate the quality factor of the resonances. Both the 5 and 3.5 μm microrings are simulated, and the results obtained for the two cases are summarized in Table I. The frequencies of the transmission minima ($g=0.25$ μm) are also included for comparison purposes.

By comparing the resonant wavelengths of the eigenvalue simulations with those of the transmission minima in the harmonic propagation analysis of Secs. III A and III B, we find an offset of 2–5 nm. This offset can be attributed to the coupling-induced frequency shift (CIFS).[22] Specifically, the presence of the bus waveguide results in a shift (decrease) in the resonant wavelengths. In other words, the resonance condition $\theta=m2\pi$ that holds in the case of the uncoupled resonator is modified to $\theta-\theta_{\mathrm{CIFS}}=m2\pi$ when the ring becomes coupled to the waveguide. As is evident from Eq. (2), $\theta_{\mathrm{CIFS}}=\theta_0-\theta_t$. To confirm this assumption we can follow two different routes. We can first consider the aggregate eigenvalue problem of ring and bus, thus incorporating the CIFS in the simulation. By doing so, the first resonant wavelength of the 3.5 μm ring is found to be equal to 1.519 μm (instead of 1.522 μm for the uncoupled ring), as is also predicted by the harmonic propagation simulations. Alternatively, we can perform a harmonic propagation simulation of a microring resonator filter having a large gap (e.g., 0.7 μm), separating the bus waveguide from the ring. This way the coupling between the two is greatly reduced, and the frequencies of the transmission minima approach the resonant frequencies of the uncoupled microring. Indeed, the wavelength of the first transmission minimum in this case is found to be 1.521 μm.

TABLE I. Resonant wavelengths and respective quality factors for the resonances of microring resonators with radii of both 5 and 3.5 μm. The wavelengths of the transmission minima ($g=0.25$ μm) are also included for easy reference.

Resonance[a]	52[b]	50[b]	48[b]	36[c]	34[c]
Res. wavelength (μm)	1.497	1.546	1.598	1.522	1.595
Transm. minima (μm)	1.495	1.543	1.594	1.519	1.590
Q_{tot}	220	199	175	96	72
$Q_{\mathrm{bend\ loss}}$[d]	942	635	438	144	96
$Q_{\mathrm{resist\ loss}}$	287	290	291	288	288

[a]The resonances are identified through the number of half-wavelengths that are encountered along an azimuthal roundtrip.
[b]Resonances of the 5 μm radius ring.
[c]Resonances of the 3.5 μm radius ring.
[d]A purely real dielectric permittivity for gold was adopted.

Next, we focus our attention on the quality factors of the resonances. It is clear that there are two distinct loss mechanisms present in the DLSPP-based microring resonators: resistive losses in the metallic film and bend losses, i.e., power leaving the resonator by coupling to radial outward-going radiation modes. To distinguish between the two we perform additional simulations adopting a purely real dielectric permittivity for gold. In this case, the quality factors reflect the bend losses alone. Subsequently, the contribution of the resistive losses is calculated through

$$\frac{1}{Q_{\mathrm{tot}}}=\frac{1}{Q_{\mathrm{bend\ loss}}}+\frac{1}{Q_{\mathrm{resist\ loss}}}. \tag{4}$$

As is evident from Table I, in the 5 μm ring the resistive losses dominate while it is the bending losses that are dominant in the 3.5 μm ring. In total, the ring of smaller radius appears to exhibit higher losses and consequently a smaller quality factor. Moreover, a trend of increasing quality factor with frequency is revealed. We can explain this in terms of both resistive and bend losses. As far as the resistive losses are concerned, the imaginary part of the dielectric permittivity of gold decreases with frequency and therefore resistive losses are lowered. Regarding bend losses, with increasing frequency the TM_{00} mode becomes more confined, resulting in lower bend losses as well.

TABLE II. Material properties adopted in the thermal modeling simulations.

Material	K [a] [W/(m K)]	ρ [b] (kg/m^3)	C_p [c] [J/(kg K)]
Silicon (Si)	145	2 330	700
Silica (SiO_2)	1.1	2 200	703
Gold (Au)	120	19 300	129.1
Polymer	0.2	1 200	1000

[a]Thermal conductivity.
[b]Density.
[c]Specific heat capacity at constant pressure.

IV. THERMAL TUNING

A tunable/switching element can be realized by taking a wavelength-selective component and providing the ability to tune its resonant wavelength by means of a control signal. Currently, the sole tuning mechanism readily available in plasmonics is the one relying on the thermo-optic effect. Components based on the DLSPP waveguide naturally allow for external control through the thermo-optic effect by injecting in the metallic film—that must be restricted to a finite width therefore becoming a stripe—an electric current that changes the local temperature and eventually the refractive index of the thermo-optic polymer residing on top. Ultimately, the resonant wavelength of the wavelength-selective component incorporating the thermo-optic polymer is tuned. It is worth noting that the implementation of the DLSPP-based thermally controlled components can be quite efficient due to the field enhancement near the metal-dielectric interface (Fig. 2). The temperature increase due to Ohmic heating induced by the control current injected in the metallic film is anticipated to be at its maximum near that same interface too.

The thermo-optic effect has been employed in the implementation of various dynamic components based on the stripe plasmonic waveguide.[23,24] However, in the context of DLSPP components, thermal tuning has not yet been demonstrated. In this work, we assess the performance of thermo-optic control in microring resonator filters by performing thermal modeling simulations.

A. Thermal modeling

For the purpose of thermal modeling we solve the thermal diffusion equation

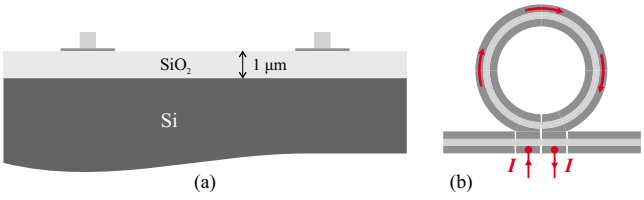

FIG. 8. (Color online) (a) Cross section of the computational domain considered in the thermal modeling simulations. (b) Possible practical layout of electrode placement resulting in an azimuthal current covering the entire circumference of the ring.

TABLE III. Average temperature increase (ΔT_{av}) for different values of the driving current.

Injected current (mA)	5	10	15	20
Current density (GA/m^2)	35.7	71.4	107.14	142.6
ΔT_{av} (K)	5.92	23.71	53.36	94.8

$$\nabla \cdot (-K \nabla T) = Q \equiv \frac{J^2}{\sigma} \tag{5}$$

by means of the nodal 3D-FEM. In the above equation, J stands for the current density. The material properties used in all simulations are those compiled in Table II. Additionally, a heat transfer coefficient h equal to 10 W/(m^2 K) has been assumed for convection with air, and the gold stripe thin film conductivity σ has been selected to be equal to 10^7 S/m.

The geometry considered in the simulations consists of a standalone DLSPP-based ring on top of a typical silicon-on-insulator (SOI) substrate [Fig. 8(a)]. The SOI substrate is chosen in view of a prospective hybridization of the two prominent technologies for nanophotonic circuits: plasmonics and silicon photonics. Such a hybridization is considered highly probable in the near future. As mentioned earlier, the metallic film is restricted into becoming a stripe. The dimensions of the stripe are 2 μm$\times$70 nm; such a modification does not affect the optical mode. An azimuthal current of constant density flows therein. The combined structure of the polymer ridge and the metallic stripe is placed on top of a 1-μm-thick silica layer with a silicon substrate and a heat sink beneath. This implies that a boundary condition of constant temperature (T=293 K) can be assigned to the bottom face of the silicon layer. Convective boundary conditions are assigned to all surfaces in contact with air.

Simulations were conducted for several values of the driving current, and the results are summarized in Table III. The maximum allowed driving current is limited by electromigration.[24] For the maximum value of 20 mA, equivalent to a current density J of 142.8 GA/m^2, the computed temperature difference ($\Delta T = T - 293$) is depicted in Fig. 9. The average, in the polymer loading, temperature difference (ΔT_{av}) is approximately 95 K. The approach of taking the average of ΔT is fully justified by the fact that ΔT is almost constant in the entire spatial extent of the loading, as is evident from Fig. 9. Therefore, ΔT_{av} is very representative

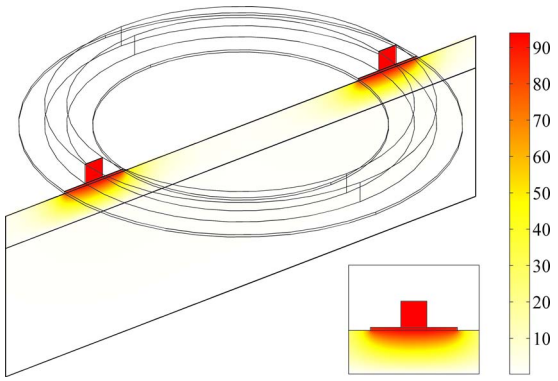

FIG. 9. (Color online) ΔT map in a slice of the 3D structure and detail showing almost constant ΔT in polymer loading.

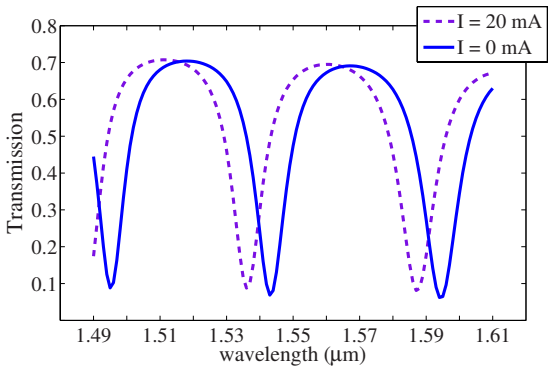

FIG. 10. (Color online) Transmission vs wavelength for the thermally tuned filter ($R=5$ μm and $g=0.25$ μm). For a driving current of 20 mA, an 8 nm shift in the transmission minima is observed.

and can be directly employed in estimating the refractive index for the subsequent optical calculations. It should be noted that as Si has a very high thermal conductivity, the temperature drop across the silicon layer is almost zero (Fig. 9).

B. Filter transmission

In this section we consider the effect of thermal tuning on the filter transmission for the case of $I=20$ mA ($\Delta T_{\mathrm{av}}=95$ K). Assuming a typical thermo-optic coefficient (TOC) of -9×10^{-5} for the polymer, we end up with a refractive index of 1.5276 instead of the value of 1.5362 that corresponds to room temperature ($T=293$ K). By subsequently appointing this modified value to the permittivity of the ring and solving the electromagnetic problem, we acquire the dashed transmission curve depicted in Fig. 10. We note that the patterning of the metallic film [Fig. 8(b)], essential for the electrical isolation of those parts addressed through the driving current, was not taken into account in the electromagnetic simulation. However, we expect that this patterning would only minimally affect the filter performance, provided that the isolation gaps introduced are small (e.g., in the order of 100 nm), and the metallic stripes are sufficiently wide to accommodate the TM_{00} mode.

A shift in the transmission minima of approximately 8 nm is observed. Obviously, for a microring resonator filter to efficiently function as a switching element its tuning capability should be equal to FSR/2, a condition that is not fulfilled in this case. However, this condition can be met by performing slight modifications to the proposed structure. Specifically, a polymer with a higher TOC and a more elaborate substrate configuration could possibly result in a shift of 20 nm or more. Then, a microring resonator filter having a FSR of 40 nm or less (attained with a resonator of greater circumference and possibly a racetrack shape to reduce footprint) could indeed function as an efficient switching element.

C. Temporal response

Equally important to the tuning range is the switching speed of a component intended as a switching element. Therefore, it is crucial to assess the temporal response of thermal tuning in the aforementioned configuration. This is done by solving the transient problem described by the following equation:

$$\rho C_p \frac{\partial T}{\partial t} + \nabla \cdot (-K \nabla T) = Q \equiv \frac{J^2}{\sigma}. \tag{6}$$

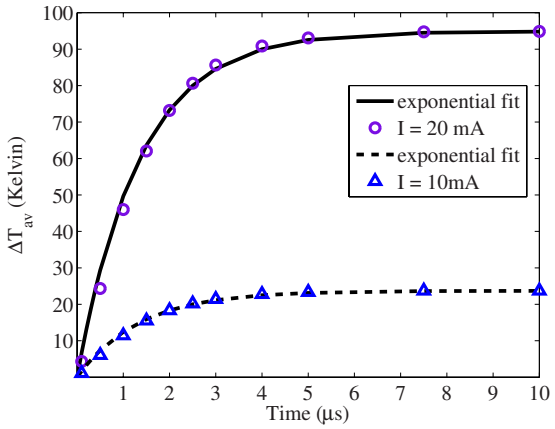

FIG. 11. (Color online) Temporal evolution of the average in the loading temperature increase for driving currents of 10 and 20 mA. Fitted curves indicate a time constant of 1.35 μs.

Again, the solution is obtained by the nodal 3D-FEM. The geometry, material properties, and boundary conditions are the same as in the steady-state case (Sec. IV A). Time stepping goes up to 10 μs in increments of 0.1 μs.

The temporal evolution of the average in the loading temperature increase is depicted in Fig. 11 for driving currents of both 10 and 20 mA. The response is primarily exponential, as indicated by the almost perfect fit that is provided, obeying

$$\Delta T_{\mathrm{av}}(t) = \Delta T_{\mathrm{av}}^{\infty}(t)(1 - e^{-t/\tau_{\mathrm{rise}}}). \tag{7}$$

A time constant τ_{rise} of 1.35 μs is extracted in both cases, fully consistent with initial closed form estimates which suggest a value of ~1 μs for this particular geometry. By turning off the current and letting the structure to cool we obtain a time constant τ_{fall} for the cooling process of ~1.35 μs as well. We should note, however, that the time constants (rise and fall) of the optical response could be somewhat different from those calculated for the averaged, in the polymer loading, ΔT.

V. SUMMARY AND CONCLUSIONS

Microring resonator filters made of DLSPP waveguides have been analyzed by means of the 3D vector finite element method. The effect of the key structural parameters on the transmission properties of the filter has been investigated. We have demonstrated that the gap mainly affects the extinction ratio, while the variation in the ring radius modifies the FSR and the linewidth of the minima when significant variations are considered. Extinction ratios as high as 17 dB have been attained with rings of both 5 and 3.5 μm. Moreover, the uncoupled microring resonator has been treated as an eigenvalue problem in an attempt to corroborate the findings of the harmonic propagation simulations. The resonant wavelengths were found to agree well with those of the transmis-

sion minima, provided that the CIFS is taken into account. The quality factors of the resonances were found to be ~200 in the 5 μm ring case and ~100 in the 3.5 μm ring case.

Furthermore, we have quantified the shift in the transmission minima when the ring's refractive index is altered by virtue of thermal tuning. A current density of 142.8 GA/m^2 was found to result in a shift of 8 nm for typical material properties. We have also assessed the switching performance of the thermally addressed filters by solving the transient thermal diffusion equation. The temporal response has been identified as being primarily exponential, and a time constant of 1.35 μs has been extracted from the exponential fit.

In Sec. IV B we have argued that with some minor modifications the thermally addressed microring resonator filter could efficiently function as a switching element. Another step in the direction of implementing DLSPP-based switching elements would be to consider resonator filters employing other types of resonators, e.g., microdisk. This could result in filters being more compact and having a broader tuning range. Finally, if faster switching times are required one could turn to different kinds of addressing, such as electro-optic and/or all optical.

[1]H. Raether, *Surface Plasmons on Smooth and Rough Surfaces and on Gratings* (Springer-Verlag, Berlin, 1988).
[2]W. L. Barnes, A. Dereux, and T. W. Ebbesen, Nature (London) **424**, 824 (2003).
[3]S. A. Maier and H. A. Atwater, J. Appl. Phys. **98**, 011101 (2005).
[4]R. Zia, J. A. Schuller, A. Chandran, and M. L. Brongersma, Mater. Today **9**, 20 (2006).
[5]E. Ozbay, Science **311**, 189 (2006).
[6]T. W. Ebbesen, C. Genet, and S. I. Bozhevolnyi, Phys. Today **61**(5), 44 (2008).
[7]P. Berini, Phys. Rev. B **61**, 10484 (2000).
[8]P. Berini, R. Charbonneau, N. Lahoud, and G. Mattiusi, J. Appl. Phys. **98**, 043109 (2005).
[9]S. I. Bozhevolnyi, V. S. Volkov, E. Devaux, and T. W. Ebbesen, Phys. Rev. Lett. **95**, 046802 (2005).
[10]K. C. Vernon, D. K. Gramotnev, and D. F. P. Pile, J. Appl. Phys. **103**, 034304 (2008).
[11]C. Reinhardt, S. Passinger, B. N. Chichkov, C. Marquart, I. P. Radko, and S. I. Bozhevolnyi, Opt. Lett. **31**, 1307 (2006).
[12]B. Steinberger, A. Hohenau, H. Ditlbacher, A. L. Stepanov, A. Drezet, F. R. Aussenegg, A. Leitner, and J. R. Krenn, Appl. Phys. Lett. **88**, 094104 (2006).
[13]T. Holmgaard and S. I. Bozhevolnyi, Phys. Rev. B **75**, 245405 (2007).
[14]T. Holmgaard, Z. Chen, S. I. Bozhevolnyi, L. Markey, A. Dereux, A. V. Krasavin, and A. V. Zayats, Opt. Express **16**, 13585 (2008).
[15]A. V. Krasavin and A. V. Zayats, Phys. Rev. B **78**, 045425 (2008).
[16]Z. Chen, T. Holmgaard, S. I. Bozhevolnyi, A. V. Krasavin, A. V. Zayats, L. Markey, and A. Dereux, Opt. Lett. **34**, 310 (2009).
[17]T. Holmgaard, Z. Chen, S. I. Bozhevolnyi, L. Markey, A. Dereux, A. V. Krasavin, and A. V. Zayats, Appl. Phys. Lett. **94**, 051111 (2009).
[18]T. Holmgaard, Z. Chen, S. I. Bozhevolnyi, L. Markey, and A. Dereux, Opt. Express **17**, 2968 (2009).
[19]A. Yariv, Electron. Lett. **36**, 321 (2000).
[20]P. B. Johnson and R. W. Christy, Phys. Rev. B **6**, 4370 (1972).
[21]J. Jin, *The Finite Element Method in Electromagnetics*, 2nd ed. (Wiley, New York, 2002).
[22]M. A. Popović, C. Manolatou, and M. R. Watts, Opt. Express **14**, 1208 (2006).
[23]T. Nikolajsen, K. Leosson, and S. I. Bozhevolnyi, Appl. Phys. Lett. **85**, 5833 (2004).
[24]G. Gagnon, N. Lahoud, G. A. Mattiussi, and P. Berini, J. Lightwave Technol. **24**, 4391 (2006).